CHEMISTRY OF MATERIALS
Cite This: Chem. Mater. 2019, 31, 2497−2506
Article
pubs.acs.org/cm

Formation and Composition-Dependent Properties of Alloys of Cubic Halide Perovskites

Gustavo M. Dalpian,*[,†,‡] Xin-Gang Zhao,[†] Lawrence Kazmerski,[†] and Alex Zunger*[,†]

[†]University of Colorado Boulder, Boulder, Colorado 80309, United States
[‡]Centro de Ciências Naturais e Humanas, Universidade Federal do ABC, 09210-580 Santo André, São Paulo, Brazil

Supporting Information

ABSTRACT: Distinct shortcomings of individual halide perovskites for solar applications, such as restricted range of band gaps, propensity of ABX_3 to decompose into AX + BX_2, or oxidation of $2ABX_3$ into A_2BX_6, have led to the need to consider alloys of individual perovskites such as [FA,Cs][Pb,Sn][Br,I]$_3$. This proposition creates a nontrivial material selection problem associated with a six-component structure, spanning a continuum of three sets of compositions (one for each sublattice) and requiring control of phase separation or ordering in each alloyed subfield. Not surprisingly, material and structure choices were made thus far mostly via trial-and-error explorations among a large number of arrangements. Here, we use ideas from solid-state theory of semiconductor alloys to analyze the behaviors of the canonical [FA,Cs][Pb,Sn]I_3 alloy system, where FA is formamidinium. Density functional calculations utilizing specially constructed supercells are used to calculate the composition dependence of band gaps, energy of decomposition, and alloy mixing enthalpies. A number of clear trends are observed for A-site alloys [Cs,FA]SnI_3 and [Cs,FA]PbI_3, as well as for B-site alloys Cs[Sn,Pb]I_3 and FA[Sn,Pb]I_3. To understand the physical reasons that control these trends, we decompose the alloy properties into distinct physical terms: (i) the energies associated with removing the octahedral deformations (tilting, rotations, B-site displacements) of the individual components, (ii) the energies for compressing the larger component and expanding the smaller one to the alloy volume $V(x)$, (iii) the charge-transfer energies associated with placing the alloyed units onto a common lattice, and finally, (iv) structural relaxation of all bonds within the cells. This analysis clarifies the origin of the observed trends in band gaps, decomposition energies, and mixing enthalpies. Unlike a number of previous calculations, we find that the proper description of alloy physics requires that even the pure, nonalloyed, end-point compounds need to be allowed to develop local environment-dependent octahedral deformation that lowers significantly the total energy and raises their band gaps.

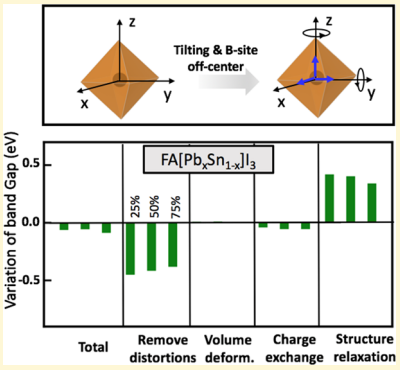

INTRODUCTION: OVERCOMING DEFICIENCIES OF INDIVIDUAL COMPOUNDS BY ALLOY FORMATION

The latest advances on the development of solar cells based on halide perovskites have shown that individual (nonalloyed) single-ABX_3 perovskites are not optimal for this kind of application. Single-ABX_3 perovskites have been demonstrated to have limited stability toward decomposition into binary constituents (i.e., $MAPbI_3$ transforming into MAI + PbI_2),[1] being prone to oxidation (i.e., $2CsSnI_3$ converting to the Sn-vacancy compound Cs_2SnI_6)[2−4] or loss of halogen,[5] possible phonon (dynamic) instability,[6−8] and often not having the ideal band gaps for tandem solar applications.[9]

Because the properties $P(x)$ of an alloy can deviate significantly from the composition (x)-weighted linear average of the respective properties of the constituents ("alloy bowing"[10,11]), the possibility is raised that alloying might solve the problems with respect to instabilities to the above-noted deficiencies. All recent record-breaking solar cells[9,12−15] were synthesized using mixtures of several perovskites instead of single compounds. This prospect of formation of alloys ("solid solutions"), such as [FA,Cs][Pb,Sn][Br,I]$_3$, among many others,[16−25] creates a nontrivial material selection problem associated with a six-component structure, spanning a continuum of compositions (x, y, and z for each sublattice) and requiring control of phase separation or ordering in each alloyed subfield. Not surprisingly, material and structure choices have been made thus far mostly via trial-and-error explorations among a large number of arrangements.[9,12−15,26] The potential for missing the best combinations or failing to apply understanding-based property optimization cannot be negligible.

We evaluate the alloy bowing for three of these properties, considering alloys based on [FA,Cs][Pb,Sn]I_3. The questions on optimizing properties by creating alloys can be illustrated as follows: (i) The $APbX_3$ compound tends to decompose into PbX_2 + AX, whereas the $ASnX_3$ compounds do not. However, the latter have a tendency to oxidize (whereby 2 formula units of $ASnX_3$ form A_2SnX_6). Are there other ways to overcome the

Received: December 26, 2018
Revised: February 27, 2019
Published: February 27, 2019

Downloaded via UNIV OF COLORADO BOULDER on August 1, 2023 at 21:33:09 (UTC).
See https://pubs.acs.org/sharingguidelines for options on how to legitimately share published articles.

© 2019 American Chemical Society

DOI: 10.1021/acs.chemmater.8b05329
Chem. Mater. 2019, 31, 2497−2506

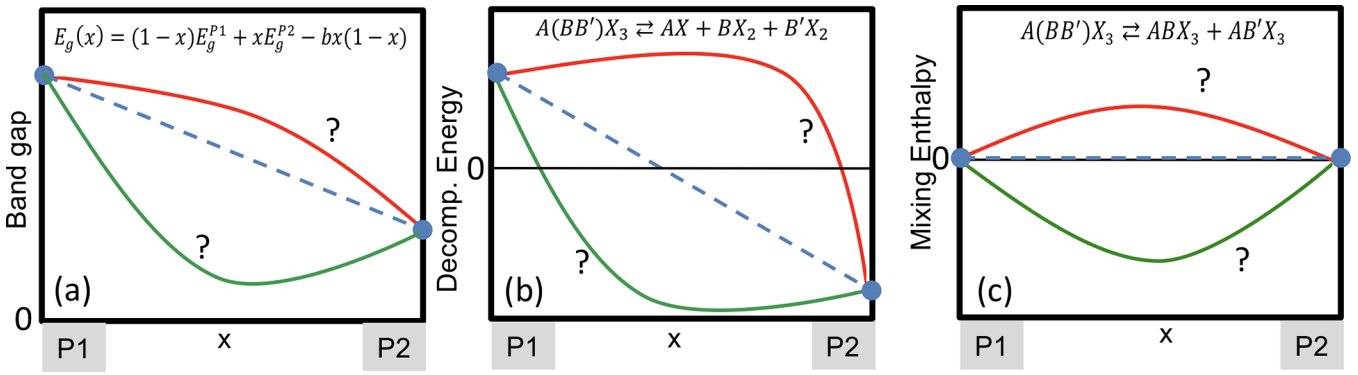

Figure 1. Schematic description of different possible bowing situations: linear (blue dashed line), positive (green solid line), and negative (red solid line) of different physical properties. The three cases are for (a) band gaps, (b) decomposition energy (ABX_3 into $AX + BX_2$), and (c) bowing of alloy mixing enthalpy.

decomposition tendency for Pb compounds? Also, (ii) the $A[B_xB'1-_x]X_3$ alloy could phase-separate below a miscibility gap (MG) temperature $T_{MG} \approx \Delta H_{mix}(x)/S$ into its alloyed constituents $xABX_3 + (1-x)AB'X_3$ if the corresponding mixing enthalpy delta-$\Delta H_{mix}(x)$ is positive.[27] Would halide perovskite alloys be resilient to phase separation at a sufficiently low T_{MG}, or would the alloy order be crystallographic below an ordering temperature T_{ord} (if delta-$H(x)$ is negative)?

The analysis of the bowing properties is made through a Born–Haber (B-H)-like cycle, in which the variation of the properties is broken into a series of sequential steps, providing understanding in finer detail for the specific behavior of the alloy.

GENERALIZED ALLOY BOWING PROBLEM

The general bowing of alloy properties, including band gaps, decomposition energy, and mixing enthalpy, is illustrated schematically in Figure 1. The dashed lines show the reference linear interpolation, whereas the red and the green curves indicate a few possible realizations for these actual bowing curves, each with different bowing parameters. From a quantitative point of view, each of these properties can be described as follows.

(i) Bowing of the band gaps, illustrated in Figure 1a. This is the most frequently studied deviation from linearity that is observed in alloys. For example, GaAs mixed with GaN leads[28] to large nonlinearities in the variation of the band gap as a function of concentration. We define the band gap bowing parameter b_g for a specific alloy $A(B_xB'_{1-x})X_3$ as

$$E_g(x) = (1-x)E_g[ABX_3] + xE_g[AB'X_3] - b_g x(1-x) \quad (1)$$

where $b_g > 0$ (positive bowing coefficient) leads to a downward concave $E_g(x)$. Recall that bowing is generally defined with respect to a given crystal structure at all compositions. Different bowing curves for different crystal structures are used to judge cases in which there are structural-phase transitions. The cubic (high-temperature) phase of halide perovskites holds a special place, as solar cells based on this structure tend to have "solar" gaps, whereas the low-temperature phases (orthorhombic, tetragonal) have gaps that are often too large for solar absorption.

The assumed structures have a large effect on the calculated bowing. For example, the work of Goyal et al.[29] treated noncubic cell lattice vectors for the isolated compounds (as evident, for example, from the noncubic angles between the lattice vectors), whereas their model for the cell-internal atomic positions in the alloy showed nearly ideal, weakly relaxed (nontilted or weakly tilted) octahedra and fully nontilted molecules. Such nearly undeformed structures produce a large interaction between the states of the constituents, leading to large-bowing parameters (~1.0 eV). The present work focuses the attention on bowing in cubic alloys (i.e., the cell-external lattice parameters are restricted to the cubic phase as in the physical macroscopic alloy), whereas the cell-internal atomic positions are fully relaxed (to get meaningful relaxation, one must initially nudge the atomic positions by random displacements, as described in the Methods section below). The resulting strongly relaxed atomic positions (Table 1) show reduced interaction in the alloy between the states of the individual constituents, leading to much smaller bowing parameters (~0.3 eV).

Table 1. Calculated Properties of Single (Nonalloyed) Compounds[a]

material	volume (Å^3/f.u.)	band gap (eV)	decomposition energy (meV)	Q_B (Å)	$\lvert\Delta\theta\rvert$ (°)
$CsSnI_3$	234.6	0.91	−157	0.10	9
$CsPbI_3$	246.9	1.86	−98	0.07	10
$FASnI_3$	252.0	0.94	23	0.69	7
$FAPbI_3$	261.7	1.70	63	0.14	6

[a]Including equilibrium volume for the monomorphous (single formula unit) structure, band gap of the polymorphous phase, decomposition energy, and average distortions in the polymorphous phase, including B-site off-center distortion (Q_B) and absolute octahedra tilting angle ($\lvert\Delta\theta\rvert$) with respect to perfect structure (no distortion).

(ii) Bowing of the decomposition energy, related to the transformation of the ternary halide perovskite ABX_3 into binary compounds such as AX and BX_2, as presented in Figure 1b. This is what has been experimentally observed in calorimetric studies.[1] The general way of evaluating the decomposition energy of an alloy is

DOI: 10.1021/acs.chemmater.8b05329
Chem. Mater. 2019, 31, 2497−2506

$$\Delta H_D[A(B_xB'_{1-x})X_3] = E[A(B_xB'_{1-x})X_3] - E[AX] - (1-x)E[B'X_2] - xE[BX_2] \quad (2)$$

Here, $E[Q]$ is the total energy of compound Q, and the positive values of the decomposition energy mean that there is a tendency for the compound to decompose into the binaries. The respective bowing parameter (b_{dec}) can be obtained by fitting the curve shown in Figure 1b to the following relationship

$$\Delta H_D(x) = (1-x)\Delta H_D[AB'X_3] + x\Delta H_D[ABX_3] - b_{dec}x(1-x) \quad (3)$$

(iii) Bowing of the alloy mixing enthalpy: The mixing enthalpy measures the tendency of the alloy $A(B,B')X_3$ to phase-segregate into its parent compounds ABX_3 and $AB'X_3$, as shown in Figure 1c. When this quantity is positive, we expect phase separation, whereas when it is negative, we expect ordering. This is the traditional way to account for the stability of an alloy.[30] For an alloy with mixed A-site elements $AA'BX_3$, the mixing enthalpy is calculated as

$$\Delta H[A_xA'_{1-x}BX_3] = E[A_xA'_{1-x}BX_3] - xE[ABX_3] - (1-x)E[A'BX_3] \quad (4)$$

We can also determine a bowing parameter b_{mix} for the mixing enthalpy that can be obtained through the following equation

$$\Delta H(x) = (1-x)\Delta H[ABX_3] + x\Delta H[A'BX_3] - b_{mix}x(1-x) \quad (5)$$

DECOMPOSING ALLOY PROPERTIES INTO INDIVIDUAL PHYSICAL MECHANISMS

We analyze the directly calculated bowing by decomposing the energy to physically recognizable steps. Figure 2 illustrates the Born–Haber-like cycle we used. It starts from two compounds (illustrated by ABX_3 and $AB'X_3$) and defines two different routes for mixing them. In the first direct route (yellow arrow), we go directly to the alloy $AB_xB'_{1-x}X_3$, comparing only the initial and final properties. In route 2 (Born–Haber-like; green arrows), we break the reaction into four different steps, the sum of which gives the same final result as in route 1. The individual steps are as follows.

Step 1: Removal of Distortions (RD). We remove all distortions present in the individual compound (tilting, rotations, B-site off-center displacements, molecular rotations), taking all atoms into a perfect cubic perovskite structure ($Pm3m$). The change in energy or the change in the physical property (band gap, decomposition energy, etc.) in this step reflects the effect of undoing octahedral deformations and molecular alignment. This step is unique to perovskites, being absent from alloys of rock salt or zinc-blende compounds that do not have corner-sharing octahedra.

Step 2: Volume Deformation (VD). We expand the volume of the smaller compound and compress that of the larger compound to fit them to the alloy volume $V(x)$, assuming the Vegard's law for the interpolation. This volume deformation (VD) step can be described by the composition-weighted sum of the partial reactions

$$ABX_3|_{a_0(ABX_3)} \rightarrow ABX_3|_{a(x)} \quad (6)$$

and

$$AB'X_3|_{a_0(AB'X_3)} \rightarrow AB'X_3|_{a(x)} \quad (7)$$

Here, the subscript "0" designates the equilibrium lattice constant. The change in physical property in this step reflects the effect of volume deformation of compounds that have no octahedral tilting, rotation, and B-site off-center.

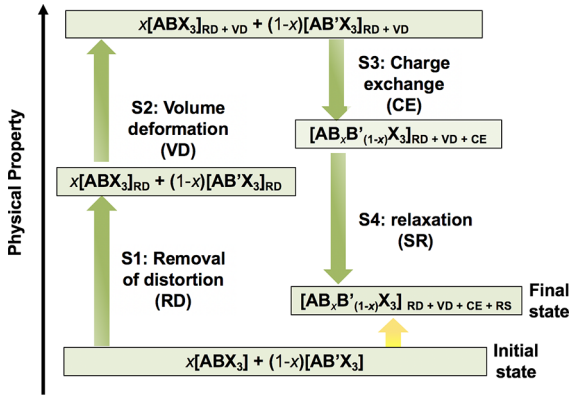

Figure 2. Schematic diagram of the Born–Haber cycle for the formation of an alloy starting from isolated nonalloyed compounds. Illustration given for mixing B-site atoms. This cycle has two different routes: route 1, indicated by the yellow arrow, goes from the initial state directly toward the final state. In route 2, indicated by green arrows, we disentangle the alloy formation into four different steps: (S1) removal of distortions (RD), (S2) volume deformation (VD), (S3) charge exchange (CE), and (S4) structural relaxation (SR).

Step 3: Charge Exchange (CE). Charge exchange (CE) represents the mixing of the previously prepared equal volume components onto a fixed lattice of the alloy. The change in physical properties is described by the formal reaction

$$(1-x)ABX_3|_{a(x)} + xAB'X_3|_{a(x)} \rightarrow AB_{1-x}B'_xX_3|_{a(x)} \quad (8)$$

Here, we join the volume-deformed structures together to form the alloy at lattice constant $a_0(x)$. At this step, the A–X and B–X bonds coexist in the alloy, and all bonds are equal to each other, while charge exchange can occur among different atomic sites. The CE step represents the effect of charge transfer from the less electronegative to more electronegative entity at a constant volume and fixed structure.

Step 4: Structure Relaxation (SR). Here, we allow all atoms to move into their minimal energy position with a fixed supercell volume after giving a random displacement on the inorganic atoms, accounting for all the distortions that are present in these compounds. This structure relaxation step is described by the formal reaction

$$AB_{1-x}B'_xX_3|_{a(x)} \rightarrow AB_{1-x}B'_xX_3|_{a(x),rel} \quad (9)$$

Note that for each composition, the different bond lengths are not single-valued but have length distributions due to the polymorphic local environment effect; that is, $R^{(n)}(x)_{A-X}$ and $R^{(n)}(x)_{B-X}$ are (n)-dependent, where n refers to a given local structure. As such, each octahedron will also have different

DOI: 10.1021/acs.chemmater.8b05329
Chem. Mater. 2019, 31, 2497–2506

volume and tilting angles. The molecules will also rotate in different orientations, according to the environment in which they are nested.

We can now write the total change in the property $P(x)$ of the alloy with respect to the composition-weighted average of the properties $P(ABX_3)$ and $P(AB'X_3)$ as a sum of four effects

$$P(x) - [xP(ABX_3) + (1 - x)P(AB'X_3)] = \Delta P_{RD} + \Delta P_{VD} + \Delta P_{CE} + \Delta P_{SR} \quad (10)$$

where the left side of the equality provides the result of the direct reaction, route 1, and the right side of the equality gives its resolution into four physical components. Constructing the change $P(x) - [xP(ABX_3) + (1 - x)P(AB'X_3)]$ obtained via route 1 is exactly the same as in route 2. The B-H cycle presented in Figure 2 can be used for all alloys that are studied here and can also be used to analyze mixing effects in most of the physical properties that are presented. In the Supporting Information, we provide tables with detailed values of the properties for all these alloys inside these B-H diagrams.

MONOMORPHOUS VERSUS POLYMORPHOUS ABX_3 NETWORKS

It has been known for a long time that octahedra in cubic perovskites can rotate and tilt. We have noted recently that the internal energy of the cubic halide perovskite phase can be lowered relative to the nominal 1-formula unit (f.u.) description of the ideal cubic structure by using a large supercell and letting each octahedron tilt, rotate, and shift its internal B-atom in a different way than other octahedra. We refer to the ensuing configuration as a polymorphous network whereby each octahedron "sees" a different local environment. This is true even for nonalloyed ABX_3. Thus, we describe even the pure ABX_3 phases as supercells of 32 f.u./cell while relaxing the cell-internal atomic positions to minimize the internal energy and keeping the cell-external lattice vectors cubic, similar to the macroscopic phase. This requires nudging of the atomic position by applying initial random displacements. Naively, one would expect that minimizing the energy of a supercell with N formula units, or a single cell with 1 formula unit, should result in the same total energy and band gaps, as is the case for ordinary compounds such as crystalline Si or III-V's. This is not the case for many cubic halide perovskites that have dynamically unstable phonons. For supercells of pure ABX_3, we find that individual octahedra tilt in different amounts on different sites, creating a range of different local environments (polymorphous network[28,31,32]) that significantly lowers the total energy and increases the band gap E_g. In this respect, we deviate from numerous previous alloy calculations, which used, for the pure phases, the ideal cubic perovskite with a minimum unit cell and its higher total energy. This alternative use of a single formula unit cell for the pure phases, the so-called monomorphous representation, leads to different mixing enthalpies on the account of the end-point compounds having artificially high energies, as discussed in the text.

DIRECT CALCULATIONS VERSUS BORN–HABER ANALYSIS OF BOWING EFFECTS IN HALIDE PEROVSKITE ALLOYS

In this section, we present our results for the different physical properties in different alloys. We first provide the direct results (route 1 in Figure 2), showing the directly calculated bowing of each property, followed by its analysis in terms of route 2: step 1 (removal of distortions), step 2 (volume deformation), step 3 (charge exchange), and step 4 (structural relaxation). Table 1 collects the basic results for the individual end-point compounds, including band gaps, equilibrium volumes, decomposition energies, and amplitude of the distortions (i.e., averaged B-site off-center displacement and averaged octahedral tilting angles) obtained from the polymorphous representation of these compounds.

Among the possible distortions, we report the following: B-site off-center displacement, related to the tendency of the B-atom (Sn or Pb) to be away from the center of the octahedra; tilting angle, related to the rotations and tilting of the octahedra compared to the perfect perovskite structure. In both cases, the magnitude of the distortion is zero for the perfect perovskites (reference).

We discuss separately the trends in the absolute values of the band gap, decomposition energies, and mixing enthalpies and then the trends in the deviations of the absolute values from a linearly weighted average (i.e., the bowing).

Trends in Absolute Values of Band Gaps versus Composition. In Figure 3, we report the results of the direct calculation of the absolute value of the band gap in the cubic phase as a function of concentration for each of the four-studied alloy systems. Dashed lines indicate the linear interpolation of the band gap. Full lines are a guide to the eye for our calculated band gaps. Bowing parameters were obtained by fitting the calculated values to eq 1.

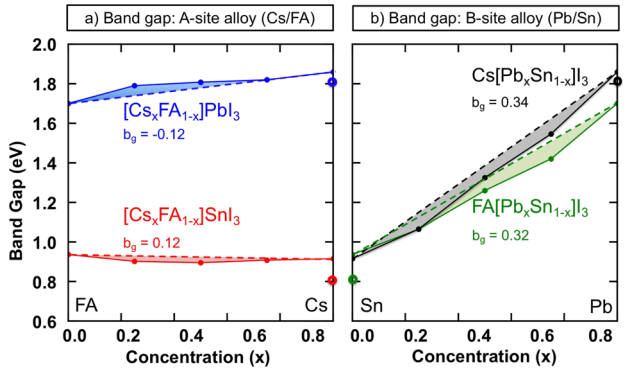

Figure 3. Variation of the band gap as a function of alloy composition for (a) mixed A-site and (b) mixed B-site alloys. All results are calculated using a polymorphous crystal structure for both alloy and end-point compounds in the cubic phase. Dashed lines indicate the linear interpolation between the limiting compounds, and solid lines are a guide to the eye. Bowing parameters, b, obtained from parabolic fits are also given. The larger circles indicate the band gap of the orthorhombic phase of the inorganic compound.

It is worth noting that, in agreement with the experiment,[33] the band gap of $CsSnI_3$ is smaller than that of $FASnI_3$, and the band gap of $CsPbI_3$ is larger than that of $FAPbI_3$. These opposing trends can be understood by noting that octahedral distortions raise the band gap and by analyzing the relative distortions for each of these compounds, as shown in Table 1. The distortions calculated for $FASnI_3$ are much larger than those of $CsSnI_3$ (mainly off-center), leading to a larger band gap in the former. On the other hand, the trend is the opposite for the Pb compounds, having larger tilting angles in the $CsPbI_3$ compound relative to $FAPbI_3$ and, consequently, larger gaps in the former.

DOI: 10.1021/acs.chemmater.8b05329
Chem. Mater. 2019, 31, 2497–2506

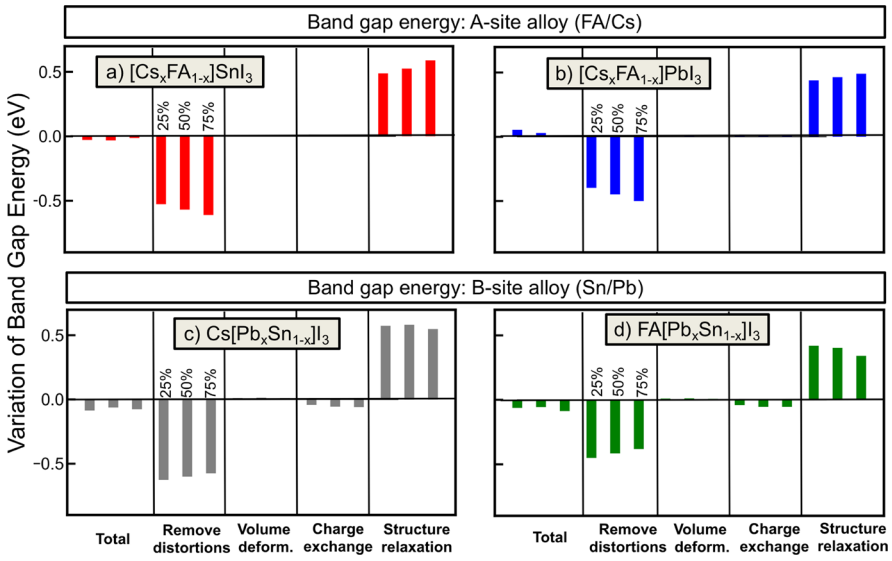

Figure 4. Decomposition of the total band gap change with respect to the composition weighted average $P(x) - [xP(ABX_3) + (1-x)P(AB'X_3)]$ into the four terms of the Born–Haber cycle $\Delta P_{RD} + \Delta P_{VD} + \Delta P_{CE} + \Delta P_{SR}$, as described in Figure 2. All results are calculated using a polymorphous crystal structure for both alloy and end-point compounds in the cubic phase. The seemingly empty bars in VD and CE represent small values. Each effect is shown at three compositions (x = 25, 50, and 75%).

Table 2. Calculated Magnitude of Octahedral Distortions in Alloy Perovskites[a]

			VBM			CBM		
materials	Q_B (Å)	$\lvert\Delta\theta\rvert$ (°)	Sn-s	Pb-s	I-p	Sn-p	Pb-p	I-p
Cs[Pb$_{0.5}$Sn$_{0.5}$]I$_3$	0.11	9	0.21	0.06	0.44	0.30	0.20	0.05
FA[Pb$_{0.5}$Sn$_{0.5}$]I$_3$	0.33	7	0.20	0.06	0.44	0.29	0.25	0.02
[Cs$_{0.5}$FA$_{0.5}$]SnI$_3$	0.32	8	0.30		0.43	0.51		0.03
[Cs$_{0.5}$FA$_{0.5}$]PbI$_3$	0.12	10		0.20	0.46		0.53	0.03

[a]Here, we report the averaged off-center displacement (Q_B) and absolute tilting angles ($\lvert\Delta\theta\rvert$) with respect to the perfect structure (no distortion). We also provide the character of the valence band maximum (VBM) and conduction band minimum (CBM).

The basic trends in the absolute values of the gaps seen in Figure 3 are as follows:

(i) Alloys on the A-sublattice have negligible composition variation in the absolute values of the band gap simply because the orbitals in the A-sublattice, be that Cs or molecules, are energetically far-removed from the frontier orbitals of the B- and X-atoms.

(ii) In contrast, alloying on the B-sublattice has a major effect on the absolute value of the gaps simply because the B-atom orbitals are directly involved in bonding, and the atomic reference energies of Sn and Pb are very different.

Trends in Bowing Parameters of Band Gaps. Figure 3 (shaded areas) shows the deviation of the alloy band gap from the linear average, that is, the bowing. We see that the bowing parameters are generally small positive signaling downward bowing, with the exception of [Cs,FA]PbI$_3$ that has a small negative bowing. Alloys on the A-sublattice have smaller bowing than those on the B-sublattice.

A direct comparison of these bowing parameters with experiment, however, is complicated by the fact that, experimentally, one generally mixes measured gaps of different crystal structures at different compositions where phase transitions from cubic to orthorhombic occur.[33] When we add our calculated band gaps of the orthorhombic phases (circles on the far right of Figure 3) to the rest of the calculated cubic values, it is clear that the effective bowing parameter changes. We conclude that the bowing parameters of the intrinsic cubic phases are small. Larger observed anomalous band gap bowing should be mostly related to structural changes, similar to what has been proposed before for $(FAPbI_3)_x(CsSnI_3)_{1-x}$,[34] where $FAPbI_3$ is mixed with $CsSnI_3$ and a transition from cubic to orthorhombic is observed.

Figure 4 provides the variation $P(x) - [xP(ABX_3) + (1-x)P(AB'X_3)]$ for the band gap of the alloys in terms of the four contributions defined in the Born–Haber cycle ($\Delta P_{RD} + \Delta P_{VD} + \Delta P_{CE} + \Delta P_{SR}$). For each alloy, the first panel of the figure presents the total band gap change, as indicated in route 1, whereas the change in the band gap owing to the other contributions is denoted in the following panels.

We noticed the following:

(i) The generally small band gap bowing in halide perovskite alloys results from vanishingly small volume deformation (VD) and charge exchange (CE) contributions and the effective compensation of removals of octahedral distortions (RD) versus the bond relaxation (SR) in the alloy. Regarding the latter compensation, the (positive) SR effect is smaller in magnitude than the (negative) RD effect, so the net change $P(x) - [xP(ABX_3) + (1-x)P(AB'X_3)]$ is negative.

(ii) Contrary to the alloys of conventional semiconductors, in which the VD term is dominant[28] so that alloys of ~2–5% lattice constant mismatch have very large bowing, in the corresponding perovskites, there is a strong strain relief in terms of the distortions of the corner-sharing octahedra

DOI: 10.1021/acs.chemmater.8b05329
Chem. Mater. 2019, 31, 2497–2506

that obviate the effects of strain. This is represented by the small VD term and the effective compensation of RD and SR.

(iii) The larger bowing in the mixed B-atom alloys (Sn and Pb) than in the mixed A-site alloys (FA and Cs) results, in part, from the existence of charge exchange in the former case (open-shell Sn and Pb ions as opposed to the neutral molecules).

(iv) Regarding the role of charge separation, Goyal et al.[29] noted that there is charge separation in the alloy band edges whereby the VBM is localized on Sn-s orbitals, whereas the CBM is localized on both Pb-p and Sn-p (slightly more on Pb-p). They argued that this charge separation explains the large (~1.0 eV) bowing parameters they calculated because the VBM inherits its character from $ASnX_3$ and the CBM inherits its character from $APbX_3$. Our calculation shows a significant charge separation (see Table 2), but we do not find large bowing for the cubic alloy (see Figure 3). Hence, charge separation cannot be the cause of bowing magnitude.

The Born−Haber analysis of Figure 4 provides the full analysis of the bowing. We observe from Figure 4 that the RD + VD + CE steps produce almost zero bowing, and it is the last step of structural relaxation (SR) that gives the final small nonzero bowing. In fact, because we use the minimum-energy polymorphous representation both for the alloy and pure compounds, we find significant octahedral distortions both for the pure compounds and alloy. So, the total bowing, being a differential quantity, is rather small. Furthermore, the charge separation seen in the alloy is not necessarily inherited from the constituents because, in our calculation, both are deformed.

Trends in Absolute Values of Decomposition Energies versus Composition. The decomposition into binary compounds is an important cause of instability in single-ABX_3 halide perovskites and has been accessed experimentally by using calorimetric methods, as recently shown for $MAPbI_3$.[1] This specific material has been shown to be unstable with respect to decomposition, with a measured formation enthalpy (or decomposition energy as defined in this paper) of 357 meV/f.u.

Table 1 provides the decomposition energies of the end-point compounds. Positive decomposition energies signal decomposition, whereas negative values imply no decomposition. We see that FA compounds are predicted to decompose, whereas Cs compounds should not. For the same A- and X-atoms, Sn compounds are more resilient to decomposition than Pb compounds. We have reported this previously,[35] and this result can be understood by the increased stability of the PbI_2 binary and the fact that the large FA molecules increase the lattice parameters, weaken the B−X bonds, and destabilize these compounds. The absolute values of the decomposition energies are shown in Figure 5, together with the respective bowing coefficients. Dashed lines indicate the linear interpolation among limiting compounds. From these data, the following items are clear:

(i) Pb-based compounds are more likely to decompose than Sn-based compounds.

(ii) Cs-based compounds are less prone to decomposition than FA-based ones.

(iii) The alloying of Cs ions into the FA-based compounds makes the compound more resistant to decomposition. In the presence of Cs, all Sn−Pb alloys will not decompose.

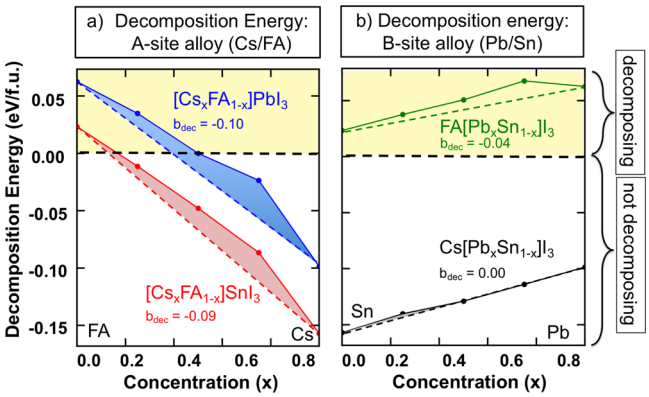

Figure 5. Variation of the absolute decomposition energy as a function of alloy composition for (a) mixed A-site and (b) mixed B-site alloys. All results are calculated using a polymorphous crystal structure for the cubic phase. Dashed lines indicate the linear interpolation among the limiting compounds, and solid lines are a guide to the eye. The bowing parameter is obtained by fitting the results to eq 3. The yellow shading indicates positive decomposition energies, that is, where the sample will break into AX + BX_2.

(iv) The inclusion of small FA concentrations leads to a large increase in the tendency toward decomposition of the compounds. In the presence of FA, all Sn−Pb alloys are decomposing.

Trends in Bowing Parameters of Decomposition Energies. The calculated bowing coefficients of the decomposition energy are larger for A-site alloys than for B-site alloys.

While the results clearly indicate that alloying is a good way to make a compound more stable with respect to decomposition, they also show that, for B-site alloys, this will not be sufficient to qualitatively change one material from being unstable to stable. It is likely that, to stabilize Pb compounds with respect to decomposition, one needs to enhance the Cs alloying.

Figure 6 provides the variation $P(x) - [xP(ABX_3) + (1 - x)P(AB'X_3)]$ for the alloy decomposition energies in terms of the four contributions ($\Delta P_{RD} + \Delta P_{VD} + \Delta P_{CE} + \Delta P_{SR}$). Here again, the VD and CE contributions are negligible, whereas the (negative) SR term is smaller in magnitude than the (positive) RD term, so the net effect on $P(x) - [xP(ABX_3) + (1 - x)P(AB'X_3)]$ is small positive. The removal of deformations (RD) causes an increase in the total energy of the compound (less stable), so decomposition becomes a likely channel. For this step, the change in the decomposition energy is larger for compounds that have organic molecules, since this large cation must fit into the restricted space of the cuboctahedral site.

Trends in Absolute Values of Alloy Mixing Enthalpy versus Composition. Special attention must be devoted to the calculation and interpretation of alloy mixing enthalpy, mainly related to the choice of the structural description of the end-point compounds used to plot the energy differences in Figure 8. If one uses, as a reference for the pure compounds, a monomorphous representation, usually represented by a cubic, single formula unit cell, this will lead to artificially negative values of the mixing enthalpies, concluding in favor of an ordering tendency for these systems. If we use a polymorphous representation instead, simulated by supercells where a random displacement is given to the inorganic parts of the compounds before relaxation, then we will have lower total energies to the limiting compounds, leading to positive mixing enthalpies for the alloy, predicting phase separation. This is

DOI: 10.1021/acs.chemmater.8b05329
Chem. Mater. 2019, 31, 2497−2506

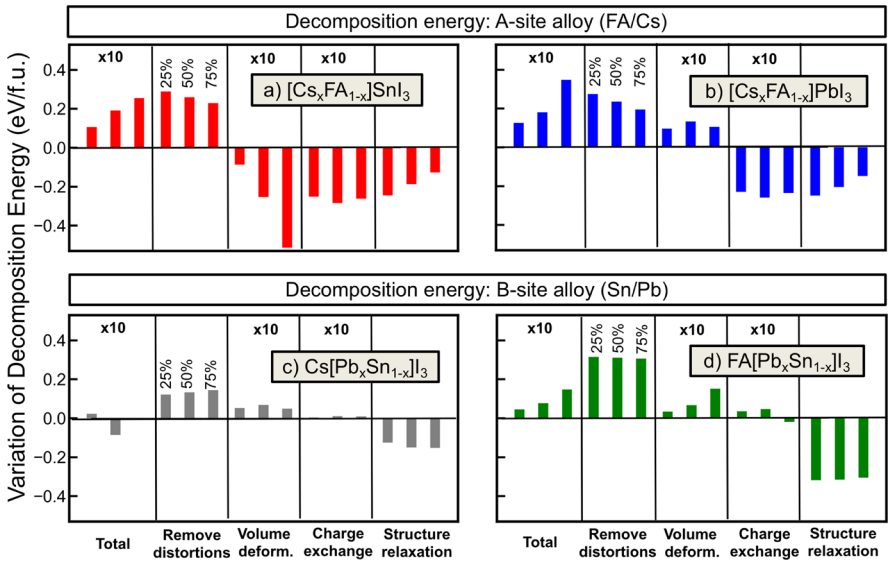

Figure 6. Breakdown of the decomposition energy of the alloy into its binary components (e.g., AX + BX_2) with respect to the composition-weighted average into the four terms $\Delta P_{RD} + \Delta P_{VD} + \Delta P_{CE} + \Delta P_{SR}$, as shown in Figure 2. All results are calculated using a polymorphous crystal structure for both the alloy and end-point compounds in the cubic phase. Each effect is shown at three compositions (x = 25, 50, and 75%). Note that the absolute value of the bars has been multiplied by a factor of 10 in some of the panels.

evidenced in Figure 7, in which the mixing enthalpy is determined as a function of concentration using two different configurations for the simulated materials. The solid curves represent energies calculated for the monomorphous structures. The calculated result is negative, indicating ordering. The dashed lines indicate the mixing enthalpy calculated using the polymorphous configurations, leading to positive mixing enthalpies. Because the polymorphous representation of the end-point compound gives a lower total energy than the monomorphous representation, we judge the latter to be the correct choice. Literature calculations show both positive and negative results for mixing enthalpies in alloy perovskites for A-site,[36] B-site,[29] and X-site[37] alloys. This suggests the possibility that perhaps monomorphous representation might have been used as the reference for the limiting compounds.

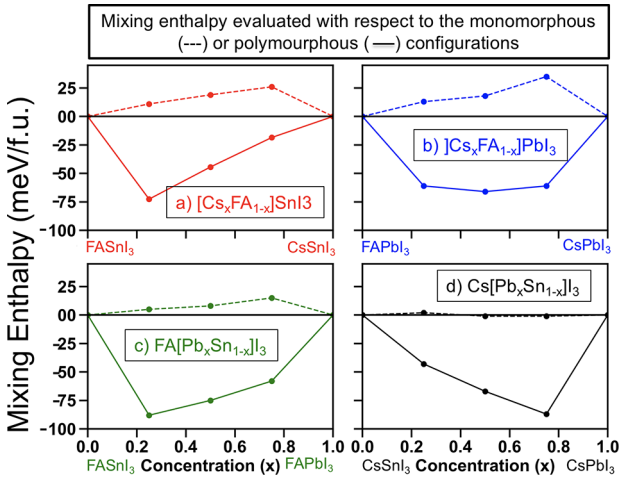

Figure 7. Mixing enthalpy as a function of composition calculated in two ways: One way is to use a minimal cell of 1 f.u. in the ideal cubic structure (monomorphous representation) for the end-point individual perovskites, shown as solid lines, with negative mixing enthalpies implying long-range ordering at low temperatures. The correct way is to use a large supercell (polymorphous representation) for the end-point compounds, same as used for the alloy, allowing it to relax under constraint of cubic lattice. This gives the results shown by the dashed lines (positive mixing enthalpies signaling phase separation).

As shown in Figure 8, although the positive results for the mixing enthalpy are an indication that phase separation should occur, one also can note that these values are very small. So, the miscibility gap temperature will be proportionally small. Bowing parameters can be as large as 0.1 eV for A-site alloys, indicating that alloying the A-site induces stronger distortions on the compounds than in B-site alloys. Similar to the case of the dissociation energy, the inclusion of a small fraction of FA molecules into the inorganic compounds leads to a strong destabilization of the material. This occurs because the lattice parameters are mostly determined by the inorganic Cs anions,

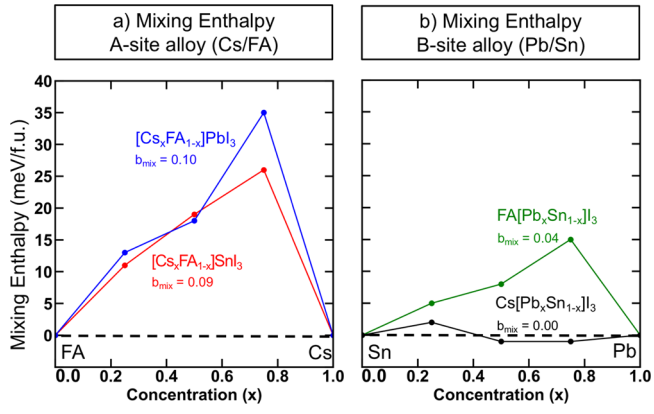

Figure 8. Variation of the mixing enthalpy as a function of alloy composition for (a) mixed A-site and (b) mixed B-site alloys. All results are calculated using a polymorphous crystal structure for the cubic phase. Dashed lines indicate the linear interpolation among the limiting compounds, and solid lines are a guide to the eye. Bowing parameters obtained by fitting eq 5 are also indicated. Positive values indicate the tendency for phase separation.

DOI: 10.1021/acs.chemmater.8b05329
Chem. Mater. 2019, 31, 2497−2506

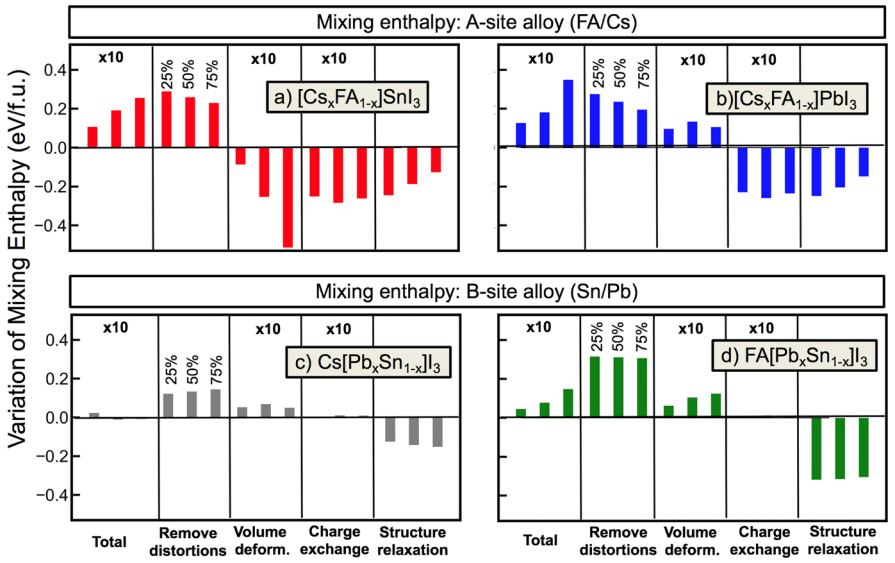

Figure 9. Decomposition of the mixing enthalpy with respect to the composition-weighted average into the four terms $\Delta P_{RD} + \Delta P_{VD} + \Delta P_{CE} + \Delta P_{SR}$, as described in Figure 2. All results are calculated using a polymorphous crystal structure for both the alloy and end-point compounds in the cubic phase. Each effect is shown at three compositions (x = 25, 50, and 75%).

leaving small spaces to fit the large FA molecules, leading to an increase in the energy of the compound.

Trends in Bowing of Mixing Enthalpy. The variation $P(x) - [xP(ABX_3) + (1 - x)P(AB'X_3)]$ for the mixing enthalpies in terms of the four contributions $\Delta P_{RD} + \Delta P_{VD} + \Delta P_{CE} + \Delta P_{SR}$ is presented in Figure 9. The effect of removing the distortions is a large increase in the mixing enthalpy, similar to the case of the decomposition energy. Removing these distortions, and consequently going to a monomorphous representation, largely increases the total energy of the system.

The effect of volume deformation will depend on the specific characteristics of each compound. As the previous step changed the potential energy surface where this material is nested, in the new potential energy surface, the material might be in the minimum volume or not. If the minimum energy volume is still the same, the contribution will be positive. If the minimum changes, the energy might decrease.

The third step of the B-H cycle is charge exchange, coming from the chemical mixture of the compounds. The change in mixing enthalpy owing to charge transfer is much larger in A-site alloys than in B-site alloys.

The last step is structural relaxation and is mostly a compensation of the first step. It always leads to a very large negative contribution, owing to the large total energy decrease it induces in the system. For the case of [Cs,FA]SnI$_3$, the total change in mixing enthalpy is positive; the only step that has a positive contribution in the decomposed cycle is RD, indicating that this is the dominant effect. The interpretation of this is that the FA molecules have more freedom to move inside the pure compounds that on alloys, restricting the energy gain in this case and leading to positive mixing enthalpy. For the case of Cs[Pb,Sn]I$_3$, on the other hand, the bowing parameter is basically zero because both the alloy and pure compounds have the same ability to relax (no organic molecules), making the contribution of RD and SR basically the same. The order of the mixing enthalpies, that is, [Cs,FA]PbI$_3$ > [Cs,FA]SnI$_3$ > FA[Pb,Sn]I$_3$ > Cs[Pb,Sn]I$_3$ can be understood by the compensation among SR and RD; the difference among both is smaller for Cs[Pb,Sn]I$_3$, followed by FA[Pb,Sn]I$_3$, [Cs,FA]SnI$_3$, and [Cs,FA]PbI$_3$.

CONCLUSIONS

Building alloys of perovskite compounds by mixing A, B, and X elements in ABX$_3$ is a very effective way to tune the properties of these alloys. This also overcomes some drawbacks of single compounds, such as tendencies to decompose. A given property of these alloys is usually in between the properties of the limiting compounds. However, they usually deviate from a linear interpolation among the limiting cases, showing some characteristic bowing.

We have analyzed the bowing properties of these alloys by using a Born−Haber (B-H) cycle and also using a systematic approach to consider the polymorphous nature of these materials. With this B-H cycle, we can precisely track the chemical and structural origins of the bowing of a given material.

For band gaps, decomposition enthalpies, and mixing enthalpies, we observe that bowing does not come from volume deformation or charge exchange. It is a competition among the relaxation of the material in the pure compounds (RD) and alloys (SR).

We have also observed that the decomposition of Pb-based compounds can be reduced by inserting Cs into the materials with organic molecules. For the mixing enthalpy, our results indicate small positive mixing enthalpies, which should be easily overcome by temperature effects. Also, attention should be devoted to the use of a polymorphous representation for all materials, even limiting compounds, to get the correct description of the alloy.

METHODS

Alloy Structure. We model the random alloy, as well as the pure ABX$_3$, constituents by using supercells containing 32 formula units (160 atoms for all-inorganic compounds). The occupation of lattice sites by the alloyed atoms was generated via the special quasirandom structures (SQS) method,[38] which assures the best random substitutional statistics possible with a given supercell size. The SQS were generated with the ATAT code[39] considering pairs and triplets with correlations of less than 10%. The volume of the alloys was taken as

DOI: 10.1021/acs.chemmater.8b05329
Chem. Mater. 2019, 31, 2497−2506

linear interpolation of the limiting compounds (Vegard's rule). The linear variation of the lattice parameter is supported by experimental evidences for alloys of these compounds.[34] The reference volume for each compound is shown in Table 1 and calculated using a single-unit cell, as reported in ref 35. We focus our study on the cubic phase of the perovskites; that is, the overall shape of the cell was kept cubic, whereas the magnitudes of the lattice vectors were adjusted to the volume $V(x)$. All cell-internal coordinates are relaxed subject to this constrain. The force tolerance criterion for relaxation was 0.01 eV/Å. The initial geometries before relaxation were taken as the perfect cubic perovskite structure; we then provide a small random displacement on the X- and B-atoms (different for each of the *N*-independent octahedra), letting them relax to their minimal energy position. For the compounds where A = organic molecule, we selected two possible orientations ("up" or "down") for the dipole of each molecule in the supercell, and the distribution of the orientations was arranged in a random way so that the sum of all dipoles was zero. This is in agreement with recent studies showing that different pair modes, or arrangements of molecules, are possible.[40]

DFT Details. All the calculations reported here were performed using the density functional theory, using similar technical settings as in our preliminary paper.[35] We have used the projected augmented wave method (PAW) and GGA/PBE exchange correlation functional without spin−orbit coupling (SOC), as implemented in the Vienna ab initio simulation package (VASP) code.[41] Previous calculations clearly show that band gap bowing parameters are not very sensitive to the use or non-use of SOC.[29] Our PAW potentials had the following valence configuration: Cs-(s2p6s1), I-(s2p5), Sn-(s2p2), Pb-(s2p2), C-(s2p2), H-(s1), and N-(s2p3). Cutoff energies were set to 520 eV, and k-point sampling varied depending on the supercell size (gamma-point calculations for 32-formula unit supercells). We have also used the optB86b[42] van der Waals corrections.

■ ASSOCIATED CONTENT

Supporting Information

The Supporting Information is available free of charge on the ACS Publications website at DOI: 10.1021/acs.chemmater.8b05329.

Structure files of all studied alloys in VASP format (ZIP)

Tables with the data used to build Figures 4, 6, and 9 (PDF)

■ AUTHOR INFORMATION

Corresponding Authors

*E-mail: Gustavo.dalpian@ufabc.edu.br (G.M.D.).

*E-mail: alex.zunger@colorado.edu (A.Z.).

ORCID

Gustavo M. Dalpian: 0000-0001-5561-354X

Xin-Gang Zhao: 0000-0001-5817-4044

Notes

The authors declare no competing financial interest.

■ ACKNOWLEDGMENTS

The research at the University of Colorado Boulder was supported by the U.S. Department of Energy, Energy Efficiency and Renewable Energy, under the SunShot "Small Innovative Programs in Solar (SIPS)" Project number DE-EE-00081531. This work used resources of the National Energy Research Scientific Computing Center, which is supported by the Office of Science of the U.S. Department of Energy under contract no. DE-AC02-05CH11231. A portion of the research was performed using computational resources sponsored by the U.S. Department of Energy's Office of Energy Efficiency and Renewable Energy and located at the National Renewable Energy Laboratory. G.M.D. also thanks the financial support from Brazilian agencies FAPESP and CNPq.

■ REFERENCES

(1) Nagabhushana, G. P.; Shivaramaiah, R.; Navrotsky, A. Direct Calorimetric Verification of Thermodynamic Instability of Lead Halide Hybrid Perovskites. *Proc. Natl. Acad. Sci. U. S. A.* **2016**, *113*, 7717−7721.

(2) Lee, B.; Stoumpos, C. C.; Zhou, N.; Hao, F.; Malliakas, C.; Yeh, C.-Y.; Marks, T. J.; Kanatzidis, M. G.; Chang, R. P. H. Air-Stable Molecular Semiconducting Iodosalts for Solar Cell Applications: Cs2SnI6 as a Hole Conductor. *J. Am. Chem. Soc.* **2014**, *136*, 15379−15385.

(3) Qiu, X.; Cao, B.; Yuan, S.; Chen, X.; Qiu, Z.; Jiang, Y.; Ye, Q.; Wang, H.; Zeng, H.; Liu, J.; et al. From Unstable CsSnI3 to Air-Stable Cs2SnI6: A Lead-Free Perovskite Solar Cell Light Absorber with Bandgap of 1.48eV and High Absorption Coefficient. *Sol. Energy Mater. Sol. Cells* **2017**, *159*, 227−234.

(4) Dalpian, G. M.; Liu, Q.; Stoumpos, C. C.; Douvalis, A. P.; Balasubramanian, M.; Kanatzidis, M. G.; Zunger, A. Changes in Charge Density vs Changes in Formal Oxidation States: The Case of Sn Halide Perovskites and Their Ordered Vacancy Analogues. *Phys. Rev. Mater.* **2017**, *1*, No. 025401.

(5) Park, B.-w.; Kedem, N.; Kulbak, M.; Lee, D. Y.; Yang, W. S.; Jeon, N. J.; Seo, J.; Kim, G.; Kim, K. J.; Shin, T. J.; et al. Understanding How Excess Lead Iodide Precursor Improves Halide Perovskite Solar Cell Performance. *Nat. Commun.* **2018**, *9*, 3301.

(6) Yang, R. X.; Skelton, J. M.; da Silva, E. L.; Frost, J. M.; Walsh, A. Spontaneous Octahedral Tilting in the Cubic Inorganic Cesium Halide Perovskites CsSnX3 and CsPbX3 (X = F, Cl, Br, I). *J. Phys. Chem. Lett.* **2017**, *8*, 4720−4726.

(7) Yaffe, O.; Guo, Y.; Tan, L. Z.; Egger, D. A.; Hull, T.; Stoumpos, C. C.; Zheng, F.; Heinz, T. F.; Kronik, L.; Kanatzidis, M. G.; et al. Local Polar Fluctuations in Lead Halide Perovskite Crystals. *Phys. Rev. Lett.* **2017**, *118*, 136001.

(8) Marronnier, A.; Roma, G.; Carignano, M. A.; Bonnassieux, Y.; Katan, C.; Even, J.; Mosconi, E.; De Angelis, F. Influence of Disorder and Anharmonic Fluctuations on the Dynamical Rashba Effect in Purely Inorganic Lead-Halide Perovskites. *J. Phys. Chem. C* **2019**, *123*, 291−298.

(9) Eperon, G. E.; Leijtens, T.; Bush, K. A.; Prasanna, R.; Green, T.; Wang, J. T.-W.; McMeekin, D. P.; Volonakis, G.; Milot, R. L.; May, R.; et al. Perovskite-Perovskite Tandem Photovoltaics with Optimized Band Gaps. *Science* **2016**, *354*, 861.

(10) Zunger, A.; Jaffe, J. E. Structural Origin of Optical Bowing in Semiconductor Alloys. *Phys. Rev. Lett.* **1983**, *51*, 662−665.

(11) Zunger, A.; Mahajan, S. Atomic Ordering and Phase Separation in Epitaxial III-V Alloys. In *Handbook on Semiconductors*; Elsevier: Amsterdam, Netherlands, 1994; Vol. 3, p 1399.

(12) Yang, W. S.; Noh, J. H.; Jeon, N. J.; Kim, Y. C.; Ryu, S.; Seo, J.; Seok, S. I. High-Performance Photovoltaic Perovskite Layers Fabricated through Intramolecular Exchange. *Science* **2015**, *348*, 1234−1237.

(13) Ergen, O.; Gilbert, S. M.; Pham, T.; Turner, S. J.; Tan, M. T. Z.; Worsley, M. A.; Zettl, A. Graded Bandgap Perovskite Solar Cells. *Nat. Mater.* **2017**, *16*, 522−525.

(14) Bailie, C. D.; McGehee, M. D. High-Efficiency Tandem Perovskite Solar Cells. *MRS Bull.* **2015**, *40*, 681−686.

(15) Saliba, M.; Matsui, T.; Seo, J.-Y.; Domanski, K.; Correa-Baena, J.-P.; Nazeeruddin, M. K.; Zakeeruddin, S. M.; Tress, W.; Abate, A.; Hagfeldt, A.; et al. Cesium-Containing Triple Cation Perovskite Solar Cells: Improved Stability, Reproducibility and High Efficiency. *Energy Environ. Sci.* **2016**, *9*, 1989−1997.

(16) Mosconi, E.; Amat, A.; Nazeeruddin, M. K.; Grätzel, M.; De Angelis, F. First-Principles Modeling of Mixed Halide Organometal Perovskites for Photovoltaic Applications. *J. Phys. Chem. C* **2013**, *117*, 13902−13913.

DOI: 10.1021/acs.chemmater.8b05329
Chem. Mater. 2019, 31, 2497−2506

(17) Brivio, F.; Caetano, C.; Walsh, A. Thermodynamic Origin of Photoinstability in the CH3NH3Pb(I1−XBrx)3 Hybrid Halide Perovskite Alloy. *J. Phys. Chem. Lett.* **2016**, *7*, 1083−1087.
(18) Slotcavage, D. J.; Karunadasa, H. I.; McGehee, M. D. Light-Induced Phase Segregation in Halide-Perovskite Absorbers. *ACS Energy Lett.* **2016**, *1*, 1199−1205.
(19) Bechtel, J. S.; Van der Ven, A. First-Principles Thermodynamics Study of Phase Stability in Inorganic Halide Perovskite Solid Solutions. *Phys. Rev. Mater.* **2018**, *2*, 045401.
(20) Li, Z.; Yang, M.; Park, J.-S.; Wei, S.-H.; Berry, J. J.; Zhu, K. Stabilizing Perovskite Structures by Tuning Tolerance Factor: Formation of Formamidinium and Cesium Lead Iodide Solid-State Alloys. *Chem. Mater.* **2016**, *28*, 284−292.
(21) Xie, L.-Q.; Chen, L.; Nan, Z.-A.; Lin, H.-X.; Wang, T.; Zhan, D.-P.; Yan, J.-W.; Mao, B.-W.; Tian, Z.-Q. Understanding the Cubic Phase Stabilization and Crystallization Kinetics in Mixed Cations and Halides Perovskite Single Crystals. *J. Am. Chem. Soc.* **2017**, *139*, 3320−3323.
(22) Boyd, C. C.; Cheacharoen, R.; Leijtens, T.; McGehee, M. D. Understanding Degradation Mechanisms and Improving Stability of Perovskite Photovoltaics. *Chem. Rev.* 2018, DOI: 10.1021/acs.chemrev.8b00336
(23) Stoumpos, C. C.; Malliakas, C. D.; Kanatzidis, M. G. Semiconducting Tin and Lead Iodide Perovskites with Organic Cations: Phase Transitions, High Mobilities, and Near-Infrared Photoluminescent Properties. *Inorg. Chem.* **2013**, *52*, 9019−9038.
(24) Jeon, N. J.; Noh, J. H.; Yang, W. S.; Kim, Y. C.; Ryu, S.; Seo, J.; Seok, S. I. Compositional Engineering of Perovskite Materials for High-Performance Solar Cells. *Nature* **2015**, *517*, 476−480.
(25) Im, J.; Stoumpos, C. C.; Jin, H.; Freeman, A. J.; Kanatzidis, M. G. Antagonism between Spin−Orbit Coupling and Steric Effects Causes Anomalous Band Gap Evolution in the Perovskite Photovoltaic Materials CH3NH3Sn1−XPbxI3. *J. Phys. Chem. Lett.* **2015**, *6*, 3503−3509.
(26) Ono, L. K.; Juarez-Perez, E. J.; Qi, Y. Progress on Perovskite Materials and Solar Cells with Mixed Cations and Halide Anions. *ACS Appl. Mater. Interfaces* **2017**, *9*, 30197−30246.
(27) Zunger, A. Spontaneous Atomic Ordering in Semiconductor Alloys: Causes, Carriers, and Consequences. *MRS Bull.* **1997**, *22*, 20−26.
(28) Kent, P. R. C.; Zunger, A. Theory of Electronic Structure Evolution in GaAsN and GaPN Alloys. *Phys. Rev. B* **2001**, *64*, 115208.
(29) Goyal, A.; McKechnie, S.; Pashov, D.; Tumas, W.; van Schilfgaarde, M.; Stevanović, V. Origin of Pronounced Nonlinear Band Gap Behavior in Lead−Tin Hybrid Perovskite Alloys. *Chem. Mater.* **2018**, *30*, 3920−3928.
(30) Lu, Z. W.; Wei, S.-H.; Zunger, A. Long-Range Order in Binary Late-Transition-Metal Alloys. *Phys. Rev. Lett.* **1991**, *66*, 1753−1756.
(31) Dalpian, G. M.; Liu, Q.; Varignon, J.; Bibes, M.; Zunger, A. Bond Disproportionation, Charge Self-Regulation, and Ligand Holes in *s-p* and in *d*-Electron ABX_3 Perovskites by Density Functional Theory. *Phys. Rev. B* **2018**, *98*, No. 075135.
(32) Trimarchi, G.; Wang, Z.; Zunger, A. Polymorphous Band Structure Model of Gapping in the Antiferromagnetic and Paramagnetic Phases of the Mott Insulators MnO, FeO, CoO, and NiO. *Phys. Rev. B* **2018**, *97*, No. 035107.
(33) Prasanna, R.; Gold-Parker, A.; Leijtens, T.; Conings, B.; Babayigit, A.; Boyen, H.-G.; Toney, M. F.; McGehee, M. D. Band Gap Tuning via Lattice Contraction and Octahedral Tilting in Perovskite Materials for Photovoltaics. *J. Am. Chem. Soc.* **2017**, *139*, 11117−11124.
(34) Zong, Y.; Wang, N.; Zhang, L.; Ju, M.-G.; Zeng, X. C.; Sun, X. W.; Zhou, Y.; Padture, N. P. Homogenous Alloys of Formamidinium Lead Triiodide and Cesium Tin Triiodide for Efficient Ideal-Bandgap Perovskite Solar Cells. *Angew. Chem. Int. Ed.* **2017**, *56*, 12658−12662.
(35) Yang, D.; Lv, J.; Zhao, X.; Xu, Q.; Fu, Y.; Zhan, Y.; Zunger, A.; Zhang, L. Functionality-Directed Screening of Pb-Free Hybrid Organic−Inorganic Perovskites with Desired Intrinsic Photovoltaic Functionalities. *Chem. Mater.* **2017**, *29*, 524−538.
(36) Yi, C.; Luo, J.; Meloni, S.; Boziki, A.; Ashari-Astani, N.; Grätzel, C.; Zakeeruddin, S. M.; Röthlisberger, U.; Grätzel, M. Entropic Stabilization of Mixed A-Cation ABX3 Metal Halide Perovskites for High Performance Perovskite Solar Cells. *Energy Environ. Sci.* **2016**, *9*, 656−662.
(37) Yin, W.-J.; Yan, Y.; Wei, S.-H. Anomalous Alloy Properties in Mixed Halide Perovskites. *J. Phys. Chem. Lett.* **2014**, *5*, 3625−3631.
(38) Zunger, A.; Wei, S.-H.; Ferreira, L. G.; Bernard, J. E. Special Quasirandom Structures. *Phys. Rev. Lett.* **1990**, *65*, 353−356.
(39) van de Walle, A. Multicomponent Multisublattice Alloys, Nonconfigurational Entropy and Other Additions to the Alloy Theoretic Automated Toolkit. *Calphad* **2009**, *33*, 266−278.
(40) Li, J.; Järvi, J.; Rinke, P. Multiscale Model for Disordered Hybrid Perovskites: The Concept of Organic Cation Pair Modes. *Phys. Rev. B* **2018**, *98*, 045201.
(41) Kresse, G.; Furthmüller, J. Efficiency of Ab-Initio Total Energy Calculations for Metals and Semiconductors Using a Plane-Wave Basis Set. *Comput. Mater. Sci.* **1996**, *6*, 15−50.
(42) Klimeš, J.; Bowler, D. R.; Michaelides, A. Chemical Accuracy for the van Der Waals Density Functional. *J. Phys.: Condens. Matter* **2010**, *22*, No. 022201.

DOI: 10.1021/acs.chemmater.8b05329
Chem. Mater. 2019, 31, 2497−2506